Performance metrics of an optical spectral imaging system for intra-operative assessment of breast tumor margins

Torre M. Bydlon[1,*], Stephanie A. Kennedy[1], Lisa M. Richards[1], J. Quincy Brown[1,4], Bing Yu[1,4], Marlee K. Junker[1,4], Jennifer Gallagher[2], Joseph Geradts[3], Lee G. Wilke[2], Nimmi Ramanujam[1,4]

[1]*Department of Biomedical Engineering, Duke University, 136 Hudson Hall, Box 90281, Durham, NC, 27708, USA*
[2]*Department of Surgery, Duke University Medical Center, 3116 N Duke St, Durham, NC, 27704, USA*
[3]*Department of Pathology, Duke University Medical Center, DUMC 3712, Durham, NC 27710, USA*
[4]*Endls Optics, 2 Davis Dr, Research Triangle Park, NC 27709, USA*
**tmb14@duke.edu*

Abstract: As many as 20-70% of patients undergoing breast conserving surgery require repeat surgeries due to a close or positive surgical margin diagnosed post-operatively [1]. Currently there are no widely accepted tools for intra-operative margin assessment which is a significant unmet clinical need. Our group has developed a first-generation optical visible spectral imaging platform to image the molecular composition of breast tumor margins and has tested it clinically in 48 patients in a previously published study [2]. The goal of this paper is to report on the performance metrics of the system and compare it to clinical criteria for intra-operative tumor margin assessment. The system was found to have an average signal to noise ratio (SNR) >100 and <15% error in the extraction of optical properties indicating that there is sufficient SNR to leverage the differences in optical properties between negative and close/positive margins. The probe had a sensing depth of 0.5-2.2 mm over the wavelength range of 450-600 nm which is consistent with the pathologic criterion for clear margins of 0-2 mm. There was <1% cross-talk between adjacent channels of the multi-channel probe which shows that multiple sites can be measured simultaneously with negligible cross-talk between adjacent sites. Lastly, the system and measurement procedure were found to be reproducible when evaluated with repeated measures, with a low coefficient of variation (<0.11). The only aspect of the system not optimized for intra-operative use was the imaging time. The manuscript includes a discussion of how the speed of the system can be improved to work within the time constraints of an intra-operative setting.

OCIS codes: (170.0170) Medical optics and biotechnology; (230.0230) Optical Devices; (300.0300) Spectroscopy

References and links

1. L. Jacobs, "Positive margins: the challenge continues for breast surgeons," Ann. Surg. Oncol. **15**(5), 1271–1272 (2008).
2. L. G. Wilke, J. Q. Brown, T. M. Bydlon, S. A. Kennedy, L. M. Richards, M. K. Junker, J. Gallagher, W. T. Barry, J. Geradts, and N. Ramanujam, "Rapid noninvasive optical imaging of tissue composition in breast tumor margins," Am. J. Surg. **198**(4), 566–574 (2009).
3. M. C. Lee, K. Rogers, K. Griffith, K. A. Diehl, T. M. Breslin, V. M. Cimmino, A. E. Chang, L. A. Newman, and M. S. Sabel, "Determinants of breast conservation rates: reasons for mastectomy at a comprehensive cancer center," Breast J. **15**(1), 34–40 (2009).
4. A. C. Society, "Cancer Facts and Figures 2009," (2009).

#121809 - $15.00 USD Received 21 Dec 2009; revised 19 Mar 2010; accepted 20 Mar 2010; published 1 Apr 2010

5. C. Kunos, L. Latson, B. Overmoyer, P. Silverman, R. Shenk, T. Kinsella, and J. Lyons, "Breast conservation surgery achieving>or=2 mm tumor-free margins results in decreased local-regional recurrence rates," Breast J. **12**(1), 28–36 (2006).
6. P. H. M. Elkhuizen, M. J. van de Vijver, J. Hermans, H. M. Zonderland, C. J. H. van de Velde, and J. W. H. Leer, "Local recurrence after breast-conserving therapy for invasive breast cancer: high incidence in young patients and association with poor survival," Int. J. Radiat. Oncol. Biol. Phys. **40**(4), 859–867 (1998).
7. M. Clarke, R. Collins, S. Darby, C. Davies, P. Elphinstone, E. Evans, J. Godwin, R. Gray, C. Hicks, S. James, E. MacKinnon, P. McGale, T. McHugh, R. Peto, C. Taylor, Y. Wang; Early Breast Cancer Trialists' Collaborative Group (EBCTCG), "Effects of radiotherapy and of differences in the extent of surgery for early breast cancer on local recurrence and 15-year survival: an overview of the randomised trials," Lancet **366**(9503), 2087–2106 (2005).
8. A. J. Creager, J. A. Shaw, P. R. Young, and K. R. Geisinger, "Intraoperative evaluation of lumpectomy margins by imprint cytology with histologic correlation: a community hospital experience," Arch. Pathol. Lab. Med. **126**(7), 846–848 (2002).
9. A. Chagpar, T. Yen, A. Sahin, K. K. Hunt, G. J. Whitman, F. C. Ames, M. I. Ross, F. Meric-Bernstam, G. V. Babiera, S. E. Singletary, and H. M. Kuerer, "Intraoperative margin assessment reduces reexcision rates in patients with ductal carcinoma in situ treated with breast-conserving surgery," Am. J. Surg. **186**(4), 371–377 (2003).
10. C. E. Cox, N. N. Ku, D. S. Reintgen, H. M. Greenberg, S. V. Nicosia, and S. Wangensteen, "Touch preparation cytology of breast lumpectomy margins with histologic correlation," Arch. Surg. **126**(4), 490–493 (1991).
11. S. E. Singletary, "Surgical margins in patients with early-stage breast cancer treated with breast conservation therapy," Am. J. Surg. **184**(5), 383–393 (2002).
12. A. O. Saarela, T. K. Paloneva, T. J. Rissanen, and H. O. Kiviniemi, "Determinants of positive histologic margins and residual tumor after lumpectomy for early breast cancer: a prospective study with special reference to touch preparation cytology," J. Surg. Oncol. **66**(4), 248–253 (1997).
13. J. C. Cendán, D. Coco, and E. M. Copeland 3rd, "Accuracy of intraoperative frozen-section analysis of breast cancer lumpectomy-bed margins," J. Am. Coll. Surg. **201**(2), 194–198 (2005).
14. T. P. Olson, J. Harter, A. Muñoz, D. M. Mahvi, and T. Breslin, "Frozen section analysis for intraoperative margin assessment during breast-conserving surgery results in low rates of re-excision and local recurrence," Ann. Surg. Oncol. **14**(10), 2953–2960 (2007).
15. T. L. Huston, R. Pigalarga, M. P. Osborne, and E. Tousimis, "The influence of additional surgical margins on the total specimen volume excised and the reoperative rate after breast-conserving surgery," Am. J. Surg. **192**(4), 509–512 (2006).
16. J. E. Méndez, W. W. Lamorte, A. de Las Morenas, S. Cerda, R. Pistey, T. King, M. Kavanah, E. Hirsch, and M. D. Stone, "Influence of breast cancer margin assessment method on the rates of positive margins and residual carcinoma," Am. J. Surg. **192**(4), 538–540 (2006).
17. M. F. Dillon, E. W. Mc Dermott, A. O'Doherty, C. M. Quinn, A. D. Hill, and N. O'Higgins, "Factors affecting successful breast conservation for ductal carcinoma in situ," Ann. Surg. Oncol. **14**(5), 1618–1628 (2007).
18. H. M. Kuerer, "If at first or second you don't succeed: mastectomy?" Ann. Surg. Oncol. **12**(11), 864–865 (2005).
19. E. D. Kurniawan, M. H. Wong, I. Windle, A. Rose, A. Mou, M. Buchanan, J. P. Collins, J. A. Miller, R. L. Gruen, and G. B. Mann, "Predictors of surgical margin status in breast-conserving surgery within a breast screening program," Ann. Surg. Oncol. **15**(9), 2542–2549 (2008).
20. I. J. Bigio, S. G. Bown, G. Briggs, C. Kelley, S. Lakhani, D. Pickard, P. M. Ripley, I. G. Rose, and C. Saunders, "Diagnosis of breast cancer using elastic-scattering spectroscopy: preliminary clinical results," J. Biomed. Opt. **5**(2), 221–228 (2000).
21. A. S. Haka, Z. Volynskaya, J. A. Gardecki, J. Nazemi, R. Shenk, N. Wang, R. R. Dasari, M. Fitzmaurice, and M. S. Feld, "Diagnosing breast cancer using Raman spectroscopy: prospective analysis," J. Biomed. Opt. **14**(5), 054023 (2009).
22. A. S. Haka, K. E. Shafer-Peltier, M. Fitzmaurice, J. Crowe, R. R. Dasari, and M. S. Feld, "Diagnosing breast cancer by using Raman spectroscopy," Proc. Natl. Acad. Sci. U.S.A. **102**(35), 12371–12376 (2005).
23. Z. Volynskaya, A. S. Haka, K. L. Bechtel, M. Fitzmaurice, R. Shenk, N. Wang, J. Nazemi, R. R. Dasari, and M. S. Feld, "Diagnosing breast cancer using diffuse reflectance spectroscopy and intrinsic fluorescence spectroscopy," J. Biomed. Opt. **13**(2), 024012 (2008).
24. F. T. Nguyen, A. M. Zysk, E. J. Chaney, J. G. Kotynek, U. J. Oliphant, F. J. Bellafiore, K. M. Rowland, P. A. Johnson, and S. A. Boppart, "Intraoperative evaluation of breast tumor margins with optical coherence tomography," Cancer Res. **69**(22), 8790–8796 (2009).
25. M. D. Keller, S. K. Majumder, M. C. Kelley, I. M. Meszoely, F. I. Boulos, G. M. Olivares, and A. Mahadevan-Jansen, "Autofluorescence and diffuse reflectance spectroscopy and spectral imaging for breast surgical margin analysis," Lasers Surg. Med. **42**(1), 15–23 (2010).
26. G. M. Palmer, and N. Ramanujam, "Monte Carlo-based inverse model for calculating tissue optical properties. Part I: Theory and validation on synthetic phantoms," Appl. Opt. **45**(5), 1062–1071 (2006).
27. G. M. Palmer, C. Zhu, T. M. Breslin, F. Xu, K. W. Gilchrist, and N. Ramanujam, "Monte Carlo-based inverse model for calculating tissue optical properties. Part II: Application to breast cancer diagnosis," Appl. Opt. **45**(5), 1072–1078 (2006).

#121809 - $15.00 USD Received 21 Dec 2009; revised 19 Mar 2010; accepted 20 Mar 2010; published 1 Apr 2010

28. P. I. Tartter, J. Kaplan, I. Bleiweiss, C. Gajdos, A. Kong, S. Ahmed, and D. Zapetti, "Lumpectomy margins, reexcision, and local recurrence of breast cancer," Am. J. Surg. **179**(2), 81–85 (2000).
29. N. Cabioglu, K. K. Hunt, A. A. Sahin, H. M. Kuerer, G. V. Babiera, S. E. Singletary, G. J. Whitman, M. I. Ross, F. C. Ames, B. W. Feig, T. A. Buchholz, and F. Meric-Bernstam, "Role for intraoperative margin assessment in patients undergoing breast-conserving surgery," Ann. Surg. Oncol. **14**(4), 1458–1471 (2007).
30. J. E. Bender, K. Vishwanath, L. K. Moore, J. Q. Brown, V. Chang, G. M. Palmer, and N. Ramanujam, "A robust Monte Carlo model for the extraction of biological absorption and scattering in vivo," IEEE Trans. Biomed. Eng. **56**(4), 960–968 (2009).
31. C. F. Zhu, G. M. Palmer, T. M. Breslin, J. Harter, and N. Ramanujam, "Diagnosis of breast cancer using diffuse reflectance spectroscopy: Comparison of a Monte Carlo versus partial least squares analysis based feature extraction technique," Lasers Surg. Med. **38**(7), 714–724 (2006).
32. L. H. Wang, S. L. Jacques, and L. Q. Zheng, "MCML--Monte Carlo modeling of light transport in multi-layered tissues," Comput. Methods Programs Biomed. **47**(2), 131–146 (1995).
33. Q. Liu, C. F. Zhu, and N. Ramanujam, "Experimental validation of Monte Carlo modeling of fluorescence in tissues in the UV-visible spectrum," J. Biomed. Opt. **8**(2), 223–236 (2003).
34. T. L. Huston, and R. M. Simmons, "Locally recurrent breast cancer after conservation therapy," Am. J. Surg. **189**(2), 229–235 (2005).

1. Introduction

Breast conserving surgery (BCS) is a recommended treatment for early stage breast cancer and for breast cancers that have been reduced in size by neoadjuvant therapy. In BCS (also known as a partial mastectomy or lumpectomy), the surgeon attempts to excise the tumor along with a margin of normal tissue, while preserving as much of the normal breast tissue as possible. Approximately 160,000 patients are eligible for breast conserving therapy each year and as many as 20-70% of patients undergoing BCS require repeat surgeries due to a close or positive surgical margin diagnosed post-operatively [1,3,4]. The pathologic margin status is an important predictor of local recurrence of an invasive or *in situ* cancer after BCS [5,6]. Thus, complete excision of the tumor is essential to reduce the risk of recurrence [7].

Currently, surgeons do not have adequate intra-operative assessment tools to ensure that the cancer has been completely removed at the time of first surgery. The lack of this capability represents a significant unmet clinical need. Only a small number of hospitals who perform BCS (less than 5%, including the Moffitt Cancer Center in Tampa, FL and the MD Anderson Cancer Center in Houston, TX) currently utilize intra-operative cytologic or pathologic analysis of tumor margins. Touch-prep cytology is a technique in which cells on the surface of the tissue are transferred to glass slides by touching the specimen to the glass, and are then stained for pathologic observation. Touch-prep cytology allows for evaluation of the whole lumpectomy surface, albeit with a wide range of sensitivities (38-100%) and specificities (85-100%) reported in the literature [8–12]. Furthermore, this technique is time consuming, requires special expertise by a cytopathologist, and does not detect tumor cells close to the lumpectomy surface. Frozen section analysis, in which the tissue is frozen and select microscopically thin sections are cut from the specimen for pathologic observation, is a technically challenging procedure due to the significant amount of fatty tissue found in breast specimens. Sensitivity ranges in the literature from 65 to 91% and specificity ranges from 86 to 100% [11,13].

A fast, non-destructive device that could image breast tumor margins in the operating room would be highly desirable to ensure complete removal of the cancer and thus reduce the risk of local recurrence. The device needs to 1) be capable of surveying multiple margins in an acceptable amount of time (within 20 minutes which is the amount of time it takes frozen section) [14], 2) have a sensing depth of 0-2 mm (the accepted criterion for clear margins) [15–19], 3) cover a large area (the majority of margin areas range from ~10-20 cm^2 in our study), 4) image with a resolution on the order of millimeters (comparable to the thickness of bread loafed slices evaluated by pathology), and 5) effectively detect differences between benign and malignant tissues and to do this without the need for pathologic evaluation, or tissue processing.

#121809 - $15.00 USD Received 21 Dec 2009; revised 19 Mar 2010; accepted 20 Mar 2010; published 1 Apr 2010

Optical imaging of tumor margins is attractive because it can quickly sample an entire tumor margin intra-operatively without damaging the tissue. Several groups are working on optical techniques for breast tumor margin assessment. Bigio et al used reflectance spectroscopy in a preliminary study to look at *in vivo* sites on the tumor bed in 24 patients (13 cancer and 59 normal sites). They showed that using hierarchical cluster analysis, cancer and normal sites could be separated with a sensitivity of 67% and a specificity of 79% [20]. Haka et al recently published on Raman spectroscopy to prospectively examine freshly excised lumpectomy specimens, which were sliced to expose tumor sites in 21 patients (123 benign and 6 malignant tissue sites) and reported a sensitivity of 83% and a specificity of 93% [21]. Their previous retrospective study showed 94% sensitivity and 96% specificity for *ex viv*o measurements of frozen samples [22]. Volynskaya et al demonstrated the ability of diffuse reflectance spectroscopy and intrinsic fluorescence spectroscopy to differentiate various benign and malignant tissues in breast biopsies from 17 patients (95 benign and 9 malignant sites), resulting in a sensitivity of 100% and a specificity of 96% [23]. Nguyen et al demonstrated that optical coherence tomography can detect tumor margin positivity in 20 patients (9 positive and 11 negative margins) with a sensitivity and specificity of 100% and 82%, respectively [24]. Keller et al recently published work on diffuse reflectance and fluorescence spectroscopy to detect cancerous sites on breast tumor margins in 32 patients (145 normal and 34 individual tumor sites), and reported a sensitivity and specificity of 85% and 96%, respectively, for classifying individual sites [25].

Our group has developed a first-generation optical spectral imaging platform that operates in the visible spectral range (450-600 nm) to rapidly and non-destructively create molecular composition maps of the tumor margin. The technologies presented above are restricted to sampling a very small area of the margin and therefore do not have the capability to image full tumor margins which is critical for a margin assessment device. We believe that this is a differentiating feature of our technology. The optical spectral imaging platform is based on diffuse reflectance spectroscopy. Diffuse reflectance spectroscopy measures the remitted light as a function of wavelength and the magnitude and shape of the spectrum is reflective of the absorption and scattering properties of the tissue. Our group has also developed a fast, scalable Monte Carlo model [26,27] to reliably and quantitatively determine the wavelength dependent absorption and reduced scattering coefficients of the tissue (μ_a and μ_s' respectively) from the diffuse reflectance spectra measured with the optical spectral imaging system. The concentration of the absorbers can be easily derived from the absorption coefficient spectra using the Beer-Lambert equation. The primary absorbers in the breast over the visible spectral range are oxygenated hemoglobin, deoxygenated hemoglobin, and β-carotene. The primary scatterers reflected by the scattering coefficient are cells and sub-cellular organelles. These extracted parameters can be used to create maps of tissue composition of the breast tumor margins.

The optical spectral imaging device was used in a clinical study from December 2007 to June 2009 on 120 patients undergoing BCS. The purpose of the study was to determine the feasibility of the device for the detection of close/positive tumor margins in an intra-operative setting. In this study, optical spectral images were collected from 1 to 2 margins per patient. The four corners of each imaged margin were inked such that the extracted parameter maps for each margin could be compared to the overall diagnosis of that margin, based on routine margin-level pathology (this is referred to as margin-level analysis). At Duke University Medical Center (DUMC), a margin is considered positive if there are tumor cells touching ink, close if there are tumor cells within 2 mm of the ink, and negative (or clear) if tumor cells are > 2mm. In addition, 6-10 sites within each imaged margin were also randomly inked such that the extracted parameters collected from those 6-10 pixels could be directly compared with pathology (this is referred to as site-level pathology).

Wilke et al [2] reported on an initial subset of patients (n = 48) from the above study where the extracted parameter maps were used as the basis for a classification scheme to

#121809 - $15.00 USD Received 21 Dec 2009; revised 19 Mar 2010; accepted 20 Mar 2010; published 1 Apr 2010

detect margin positivity. The gold standard in this case was margin-level pathology. The classification scheme based on the extracted parameter maps accurately identified 79.4% of the pathologically close/positive margins and had a specificity of 66.7%. These close/positive margins included several types of malignancies, mainly ductal carcinoma *in situ* and invasive ductal carcinoma but also lobular cancer, lobular carcinoma *in situ*, and tubular cancer. This initial study showed that the sensitivity of the technology is comparable to currently available intra-operative margin assessment tools such as frozen section but has the benefits of not requiring any type of tissue cutting, preparation, or a pathologist in the operating room.

The goal of this paper was to establish the performance metrics of the optical spectral imaging system we have developed in a manner that is relevant to breast tumor margin assessment. Specifically, this paper quantifies important sources of systematic and random errors that could arise when the system is used in a clinical setting. The endpoints characterized in this paper are, the SNR of the system, the accuracy with which the device characterizes the composition of tumor margins, the sensing depth, the amount of crosstalk between adjacent channels of the probe, and reproducibility. The optical properties of histologically normal and malignant breast tissues obtained from the randomly inked sites (site-level analysis) served as the basis for characterizing the instrument performance metrics enumerated above. Since the clinical aspects of the study are already described by Wilke et al [2], this paper will focus more on the technological aspects of the intra-operative margin assessment project. The methods section is organized by a description of the instrumentation, as well as the clinical and pathological procedures. Next, the data analysis, experiments and simulations specifically addressed in this paper are described.

2. Methods

2.1 Instrumentation and imaging probe

A block diagram of the current clinical instrument is shown in Fig. 1. The instrument consists of a 450 Watt Xenon lamp coupled to a monochromator (Gemini 180 - Jobin Yvon Horiba) set for zero-order diffraction, a multi-channel fiber-optic imaging probe (custom built by RoMack Inc.) interfaced to a plexi-glass tissue specimen box, an imaging spectrograph (Triax 320 – Jobin Yvon Horiba), and a 2D CCD camera (CCD-1024x256-OPEN-STE – Jobin Yvon Horiba). There are 8 channels on the multi-channel probe. Each channel has a core of 19, 200 μm (NA = 0.22) illumination fibers surrounded by 4, 200 μm (NA = 0.22) collection fibers with source-detector separations spanning 0.23-1.10 mm. The typical power output at the probe tips is ~3 μW and 25 μW within a 10 nm band pass at 450 and 600 nm, respectively. The probe tips of the 8 channels are arranged in a 4x2 array with a 10 mm spacing (center to center) between each channel. The illumination fibers within each channel are continuously illuminated regardless of whether data collection is taking place.

A photo of the instrument along with a computer for instrument control and data analysis is in Fig. 2A. A tumor specimen can be placed inside the plexi-glass box and interfaced with the fiber optic probe from the side (Fig. 2B). Each hole of the plexi-glass box is 5 mm apart (center to center) and has a diameter of 3.75 mm. The imaging probe placement can be shifted by 5 mm to sample inter-leaving holes between the 10 mm channel to channel spacing. The probe covers an area of approximately 2 cm x 4 cm in 4 consecutive placements of the probe. The plexi-glass slides in 1-dimension to conform to different sized specimens.

#121809 - $15.00 USD Received 21 Dec 2009; revised 19 Mar 2010; accepted 20 Mar 2010; published 1 Apr 2010

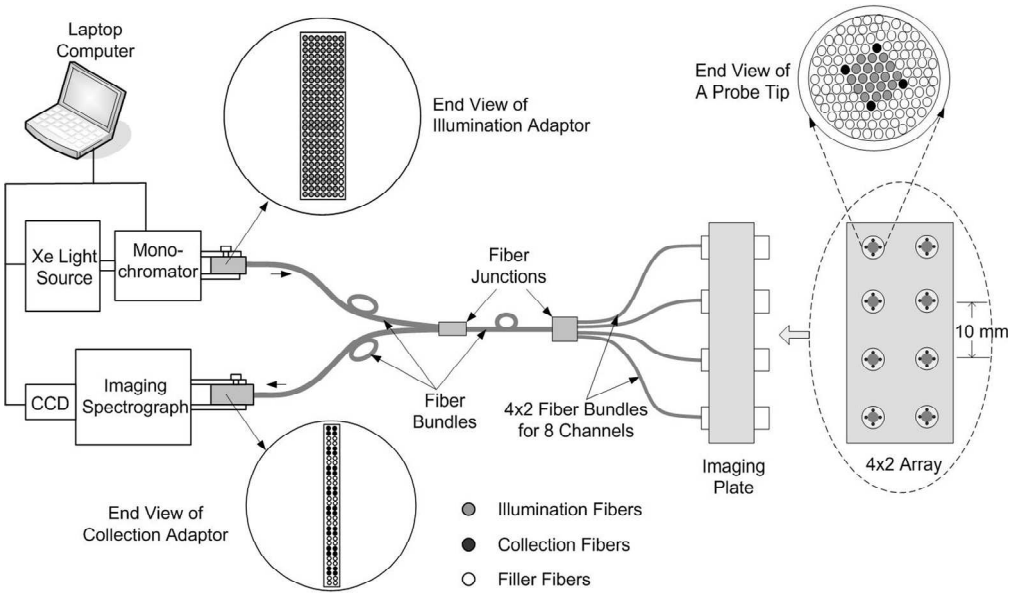

Fig. 1. Block diagram of the clinical instrument and the fiber arrangement of the multi-channel probe. Each channel has 4, 200 µm collection fibers and a central bundle of 19, 200 µm illumination fibers. All 8 channels are arranged in a 4x2 array with a separation distance of 10 mm (center to center).

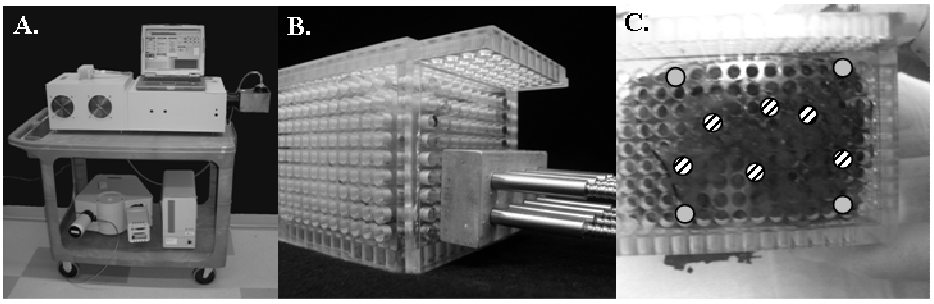

Fig. 2. A) Picture of the clinical instrument. B) Picture of the fiber optic probe in an aluminum adaptor to space each of the 8 probes 10 mm apart in a 4x2 array and the two pieces of the plexi-glass box that slide together to hold the specimen in place. C) A specimen in the plexi-glass box with light gray dots (green ink) indicating the margin border and black-white striped dots (orange ink) indicating specific sites for pathology.

2.2 Clinical procedure

A Duke Institutional Review Board approved clinical study (protocol ID – Pro00007857) to image breast tumor margins was performed on patients undergoing BCS. Partial mastectomy specimens were excised and oriented by the surgeon. For the purposes of specimen orientation, the partial mastectomy specimen was viewed as a cube. The surgeon oriented the specimen by putting sutures and/or surgical clips at the center of 4 of the 6 margins (anterior, posterior, inferior, superior, medial, and lateral). The specimen was then sent to x-ray mammography as part of the routine standard of care. After x-ray examination, the specimen was placed in the plexi-glass box (approximately 10-15 minutes post-excision) with the clip or suture at the center of the box face to maintain surgical orientation for each margin of the specimen. Diffuse reflectance measurements were collected from sites 5 mm apart until the entire margin had been scanned, taking 8 measurements simultaneously with each placement. CCD integration time was automatically set to be at the maximum end of the dynamic range.

#121809 - $15.00 USD Received 21 Dec 2009; revised 19 Mar 2010; accepted 20 Mar 2010; published 1 Apr 2010

Diffuse reflectance measurements were collected over the visible wavelength range. After all measurements were completed, the four corners of the measured margin were inked green (light gray dots in Fig. 2C) for pathological correlation with the imaged area to obtain a margin-level diagnosis by a board certified pathologist (JG). In addition, between 6 and 10 individual sites were inked orange (black-white striped dots in Fig. 2C) for separate pathological evaluation for a site-level diagnosis for use in the retrospective characterization of the instrument performance metrics. To preserve the inked areas for accurate pathological co-registration, acetic acid was applied to the specimen after inking and the specimen was wrapped in gauze to maintain the integrity of the inked areas.

2.3 Pathological evaluation

Post-operative pathology was used as the gold standard to classify each margin as negative (malignant tissue > 2 mm from tissue surface), close (malignant tissue < 2 mm from tissue surface), or positive (malignant tissue at surface). From a patient management perspective, both a positive and a close margin require re-excision. The pathologic margin status is an important predictor of local recurrence of an invasive or *in situ* cancer after BCS. The above approach is sufficiently effective to ensure complete excision of the positive margin in the second surgery in the majority of cases [19,28,29]. After the specimen was marked with ink, it was sent to surgical pathology where it was fixed overnight in 10% buffered formalin and processed in standard fashion. Specimens were bread loafed into 3 mm slices and the paraffin blocks containing the inked sites were specifically identified in the gross description. 5 µm thick sections of the partial mastectomy specimen were stained with hematoxylin and eosin (H&E) and examined by the pathologist of record, who provided a diagnosis for each measured margin (as is standard of care). In addition, the study pathologist (JG) also reviewed the inked sites microscopically to provide a histologic assessment of the underlying tissue composition of the individual sites. A qualitative assessment of the various types of tissues (fat, stroma, benign glandular tissue, carcinoma *in situ*, invasive carcinoma) was given for each site.

2.4 Data analysis for accuracy, sensing depth and crosstalk determination

Diffuse reflectance spectra were collected for two separate wavelength ranges (381-511 nm and 500-630 nm) and spliced together by averaging an 11 nm overlap to cover the entire 381-630 nm wavelength range. Diffuse reflectance spectra (450-600 nm) were corrected by CCD integration time and for daily variations in optical throughput using a Spectralon reflectance standard (LabSphere). An inverse Monte Carlo model developed by our group and described previously [26,27,30], was used to extract the optical properties (absorption and scattering) of the tissues from the integration time corrected and calibrated diffuse reflectance spectra. The inverse Monte Carlo model minimizes the sum of square of errors between a predicted diffuse reflectance spectrum and the measured spectrum by iteratively updating the optical properties. Once the sum of square errors has been minimized the concentration of absorbers, scatter size, and scatter density that are most representative of the measured tissue are computed. Using the extracted optical properties, important tissue parameters including total hemoglobin (THb) concentration, β-carotene concentration and the wavelength averaged reduced scattering coefficient from 450 to 600 nm ($<\mu_s'>$), were calculated for each measured site on the specimen surface. It took approximately 15 seconds to image and 10 seconds to process the data per placement of the probe.

The site-level data and corresponding pathology served as the basis for the retrospective characterization of the optical spectral imaging device described in this manuscript. The site-level data was used in two ways. First, the range of the tissue parameters ($<\mu_s'>$, THb, β-carotene, THb/$<\mu_s'>$, β-carotene/$<\mu_s'>$, and β-carotene/THb) was determined for all measured sites (854 sites from 104 patients). These ranges were used to make tissue mimicking phantoms to retrospectively determine the accuracy of the technology for the specific optical

#121809 - $15.00 USD Received 21 Dec 2009; revised 19 Mar 2010; accepted 20 Mar 2010; published 1 Apr 2010

properties seen in partial mastectomy specimens. Second, sites were separated by specific tissue type: positive malignant (n = 10), adipose (n = 323), fibro-glandular (n = 24), and fibro-adipose (n = 59), and the median μ_a and μ_s' at 450, 500, 550, and 600 nm were determined. This set of site-level data was used to simulate the sensing depth of the multi-channel probe and the percentage cross-talk between adjacent channels. Positive malignant sites consisted of either ductal carcinoma *in situ* (DCIS) or invasive ductal carcinoma (IDC). Close sites (disease < 2 mm from the margin) were not considered in the characterization of the system (sensing depth and cross-talk) because of their mixture of both malignant and non-malignant tissue. Close sites were considered however for the phantom studies because they are part of the full range of the measured data. The rationale for characterizing the ratios of parameters in addition to the individual parameters was that the ratios of parameters were in the classification scheme for the 48-patient study described by Wilke et al [2].

2.5 Signal-to-noise-ratio (SNR)

The signal-to-noise-ratio (SNR) of the system was calculated by taking repeated measurements (n = 6) of a Spectralon reflectance standard (LabSphere). Diffuse reflectance spectra were collected for all 8 channels. The signal level was comparable to the signal levels of the diffuse reflectance spectra collected from tissue. Spectra were corrected by integration time. The signal was calculated as the mean of the 6 measurements and noise was calculated as the standard deviation of the measurements. For each of the 8 channels, the SNR was calculated at 450 and 600 nm.

2.6 Phantom studies to determine accuracy in quantifying tissue optical properties

A tissue phantom study, as detailed by Bender et al [30] and Palmer et al [26], was conducted to assess the Monte Carlo model accuracy for extracting $<\mu_s'>$ and the concentrations of THb and β-carotene seen in the breast tumor margins. Liquid phantoms consisted of hemoglobin (H0267 Ferrous Hemoglobin, Sigma-Aldrich), 1.025μm diameter polystyrene spheres (Polysciences), and crocin (17304 Standard Fluka, Sigma-Aldrich) diluted with distilled water. Crocin (Cr) was used to mimic β-carotene since the latter is not soluble in water. As described in the Data Analysis section, the extracted tissue optical properties from all measured sites served as the basis for the absorption and scattering levels in the phantoms. Three different levels of hemoglobin concentration, β-carotene concentration and scattering were identified from the extracted optical properties measured from all sites. A total of 36 phantoms were made that represented 3 scattering levels, 3 THb concentrations at each scattering level; and 4 levels of Cr (one with no Cr) at each THb and scattering level. Diffuse reflectance measurements were made with a single channel of the probe. The purpose of this experiment was to show that tissue parameters can be extracted with reasonable accuracy for a single site on the tissue, therefore, only a single channel was used to demonstrate this, since all 8 channels have nearly identical probe geometries. The phantoms were mixed with a stir bar and plate between each measurement to maintain the homogeneity of the phantom. The data was normalized by CCD integration time, calibrated using the Spectralon standard and processed using the inverse Monte Carlo model described in the Data Analysis section. The tissue parameters (THb, $<\mu_s'>$, Cr, THb/$<\mu_s'>$, Cr/$<\mu_s'>$, and Cr/THb) extracted using the inverse Monte Carlo model were compared to expected values of the tissue parameters to assess model accuracy.

2.7 Monte Carlo simulations of sensing depth

In the *ex vivo* margin assessment study the sensing depth is a key factor in determining the feasibility of using this optical instrument as a surgical tool for detecting close and positive margins. At DUMC a clear margin is one that has a 2 mm or greater rim of normal tissue between the margin and the cancerous cells. The multi-channel probe was designed to evaluate tissue composition within 2 mm of the surface. The design was based on Monte

#121809 - $15.00 USD Received 21 Dec 2009; revised 19 Mar 2010; accepted 20 Mar 2010; published 1 Apr 2010

Carlo simulations of a previous fiber optic probe designed by our group which was found to have a sensing depth of 0.5-2 mm within homogenous tissues having a range of 0.3-20 cm^{-1} for μ_a and a range of 8.4-18 cm^{-1} for μ_s' [30,31]. In this paper, the sensing depth of each channel of the multi-channel probe was re-simulated with Monte Carlo modeling for the specific tissue optical properties of benign and positive margins as well as for non-homogeneous, layered tissue sites that are representative of close margins, by combining the optical properties of the individual tissue types. These simulations were carried out using a weighted photon Monte Carlo model, previously described by Liu et al [32,33] and Zhu et al [31]. The model records the visiting history, exit weight and maximum depth, of each photon that is detected by the collection fibers. The multi-channel probe geometry was modeled with a central illumination fiber (the composition of all the illumination fibers bundled together as one) of r = 0.515 mm, an r = 0.100 mm collection fiber, and a source-detector separation of 0.636 mm (based on the actual distance from the center of the illumination core to one of the collection fibers from a channel in the multi-channel probe). The single illumination fiber used in these simulations is equivalent in size to the 19 hexagonally packed illumination fibers of the actual multi-channel probe. An index of refraction (n) of 1.45 for the fibers and n = 1.37 for the tissue was used. The simulated homogenous medium had a thickness of 3 cm, radius of 3 cm, and was divided into grids of 0.01 cm (r) x 0.01 cm (z). Weighted visiting frequency as a function of depth was used to determine the theoretical sensing depth of the probe for the wavelengths of 450, 500, 550, and 600 nm. Visiting frequency refers to the number of times a photon visits a grid divided by the total attenuation coefficient at that grid. In order to get weighted visiting frequency, the visiting frequency is multiplied by the survival weight of the photon. Weighted visiting frequency was further normalized by the peak and sensing depth was defined as the depth at which 90% of the photons visit before being collected by the detection fiber.

Two separate simulations were run; the first was for a single-layer tissue model to determine the range of sensing depths at various wavelengths for malignant, adipose, and fibro-glandular tissue types. The optical properties for the positive sites (malignant tissue), adipose, and fibro-glandular sites were used. Fibro-adipose tissue was not used due to its similarity to adipose tissue. Close sites were excluded due to their mix in tissue composition (non-malignant and malignant tissue within the region of interest).

A second simulation was carried out for a two-layer tissue model. This model was intended to model a "close" site where there is non-malignant tissue at the margin with underlying disease less than 2 mm from the margin. Two different non-homogenous tissues were modeled with either adipose or fibro-glandular tissue for the first 1 mm layer, and both with malignant tissue for the second layer (1 mm-3 cm). Although the definition of close is between 0 and 2 mm, an average of 1 mm was used to approximate a typical close margin.

2.8 Monte Carlo simulations of cross-talk

A potential source of error arises with the simultaneous use of 8 channels and the possibility of cross-talk from adjacent channels. The current multi-channel probe was designed to have minimal cross-talk. Cross-talk can be defined in terms of a signal-to-noise ratio (SNR) and is depicted in Fig. 3. The signal is defined as the sum of the diffuse reflectance collected at C1, C2, C3, and C4 for photons launched from I6. The noise is the sum of the diffuse reflectance collected at C1, C2, C3, and C4 launched from the illumination fibers (I1-I5, I7-I8) of the 7 adjacent channels. An SNR > 100 is equivalent to less than 1% cross-talk from the adjacent channels, and is considered to be comparable to the inherent SNR of the system. Tissue cross-talk was also simulated with a Monte Carlo model [32,33]. Cross-talk is going to be worst when the tissue has a low μ_a, for any given scattering coefficient. Channels must be spaced far enough apart at the tissue surface in order to minimize cross-talk for the worst case scenario. The optical properties used in the simulation represented the lowest μ_a (found at 600 nm), along with μ_s' at the same wavelength for positive, adipose, and fibro-glandular tissue. An

#121809 - $15.00 USD Received 21 Dec 2009; revised 19 Mar 2010; accepted 20 Mar 2010; published 1 Apr 2010

illumination source (r = 0.515 mm) was modeled with 4 collection fibers (r = 0.100 mm) and separation distances (S.D.) between channels was varied from 3 to 10 mm. SNR was calculated for each separation distance for the 3 different tissue types.

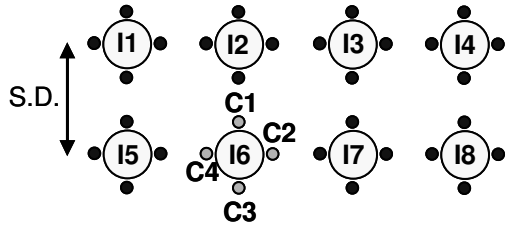

Fig. 3. The 4x2 arrangement of the fibers in the multi-channel probe to show how SNR arising from cross-talk was calculated for a channel with varying separation distances (S.D.) between channels. Light gray circles represent the illumination (I) fibers, black circles represent collection fibers for channels that contribute to the noise, and dark gray circles represent the collection (C) fibers for the channel that contributes to the signal.

2.9 Reproducibility

To test the reproducibility of the probe-tissue interface, the multi-channel probe was secured in the 4x2 array with channels spaced 10 mm apart and a partial mastectomy specimen was placed in the plexi-glass box (Fig. 2). The multi-channel probe was then interfaced with the specimen via the holes of the plexi-glass box in three different orientations: from the top of the box, the side, and bottom. Diffuse reflectance spectra were collected for each of the 8 channels. The probe was removed and placed back into the same location as the first measurement and another diffuse reflectance measurement was made. This was repeated 10 times over a period of less than 5 minutes. THb, $<\mu_s'>$, β-carotene, THb/$<\mu_s'>$, β-carotene/$<\mu_s'>$, and β-carotene/THb were extracted according to the procedures described in the Data Analysis section.

3. Results

3.1 SNR

The SNR of the clinical system is seen in Table 1. Average SNR across all channels is >100 at both 450 nm and 600 nm.

Table 1. Signal to noise ratio of each channel at 450 and 600 nm.

Channel #	SNR @ 450 nm	SNR @ 600 nm
1	340.97	45.12
2	238.46	44.58
3	162.81	113.82
4	292.61	133.56
5	167.14	97.08
6	137.08	68.29
7	131.95	248.83
8	87.62	85.75
Mean	194.83	104.63

3.2 Optical properties of breast tissue used in phantom study

The extracted values of THb, $<\mu_s'>$, β-carotene, THb/$<\mu_s'>$, β-carotene/$<\mu_s'>$, and β-carotene/THb from all measured sites (n = 854) are shown in the boxplots of Fig. 4. These plots show the empirical distribution of the data for sites on breast tumor margins, regardless

#121809 - $15.00 USD Received 21 Dec 2009; revised 19 Mar 2010; accepted 20 Mar 2010; published 1 Apr 2010

of pathology. To cover the range of data seen in the boxplots, three different levels were defined as shown in Table 2. These values were used to create the 36 phantoms with varying absorption and scattering properties which mimic the optical properties of the breast tissue. Since β-carotene is not soluble in water, crocin was used as a substitute. The extinction coefficients of β-carotene and crocin are not identical; β-carotene is ~11.6 times larger than crocin. Therefore, the absorption coefficients rather than the concentrations of β-carotene and crocin were designed to match in this study. The 3 hemoglobin levels (42.09, 64.22, and 99.81 μM) are in the upper range of the boxplot. Bender et al [30] tested phantoms with hemoglobin concentrations ranging from 1 to 35 μM and showed that the model can accurately extract absorption and scattering with accuracies of 9.8 ± 8.2% and 7.68 ± 6.3%, respectively [30]. Therefore, in this phantom study we wanted to look at higher concentrations of hemoglobin since previous studies have characterized the accuracy at lower concentrations.

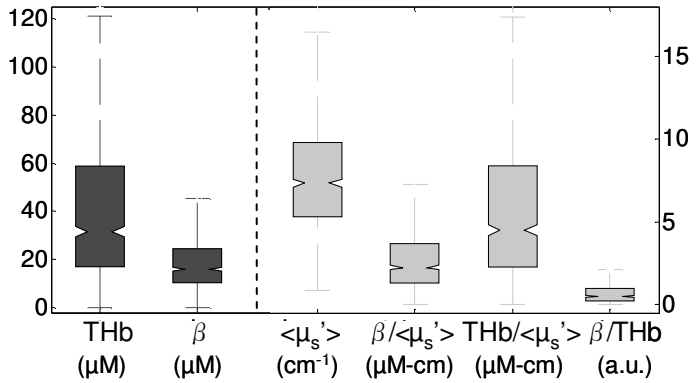

Fig. 4. Box and whisker plots of THb (μM), β-carotene (μM), $<\mu_s'>$ (cm^{-1}), β-carotene/$<\mu_s'>$ (μM-cm), THb/$<\mu_s'>$ (μM-cm), and β-carotene/THb (a.u.) for the site-level data (n = 854). The two dark gray boxplots use the y-axis on the left and the light gray boxplots use the y-axis on the right. The box represents the median, 25th percentile, and 75th percentile; the whisker represents values within 1.5 times the interquartile range.

Table 2. Values of the expected optical properties for the phantom study. β-carotene concentrations were converted into Cr concentrations by matching μ_a.

$<\mu_s'>$ (cm^{-1})	THb (μM)	β-carotene (μM)
4.85	42.09	0
6.68	64.22	10.29
9.15	99.81	16.29
		24.37

3.3 Phantom studies

The overall instrument and Monte Carlo model accuracy were assessed by evaluating the errors between the extracted and expected values seen for clinically relevant tissue parameters, taken from Table 2. The accuracy of the model at extracting hemoglobin (Hb) concentration (Fig. 5A), crocin (Cr) concentration (Fig. 5B), and $<\mu_s'>$ (Fig. 5C), along with the concentrations divided by $<\mu_s'>$ (Fig. 5D and Fig. 5E), and the ratio of crocin concentration to hemoglobin concentration (Fig. 5F) were plotted as expected data versus extracted data. As described by Palmer et al [26], the inverse Monte Carlo model uses a reference phantom to put the experimental and simulated diffuse reflectance spectra on the same scale prior to the extraction of optical properties. The best reference phantom was the one that most accurately extracted all other phantoms across a range of optical properties. In all of the plots, each circle corresponds to one phantom inverted against the best reference phantom (μ_a = 5.25, μ_s' = 5.75) from the set of 36 phantoms. The solid line in each figure

#121809 - $15.00 USD Received 21 Dec 2009; revised 19 Mar 2010; accepted 20 Mar 2010; published 1 Apr 2010

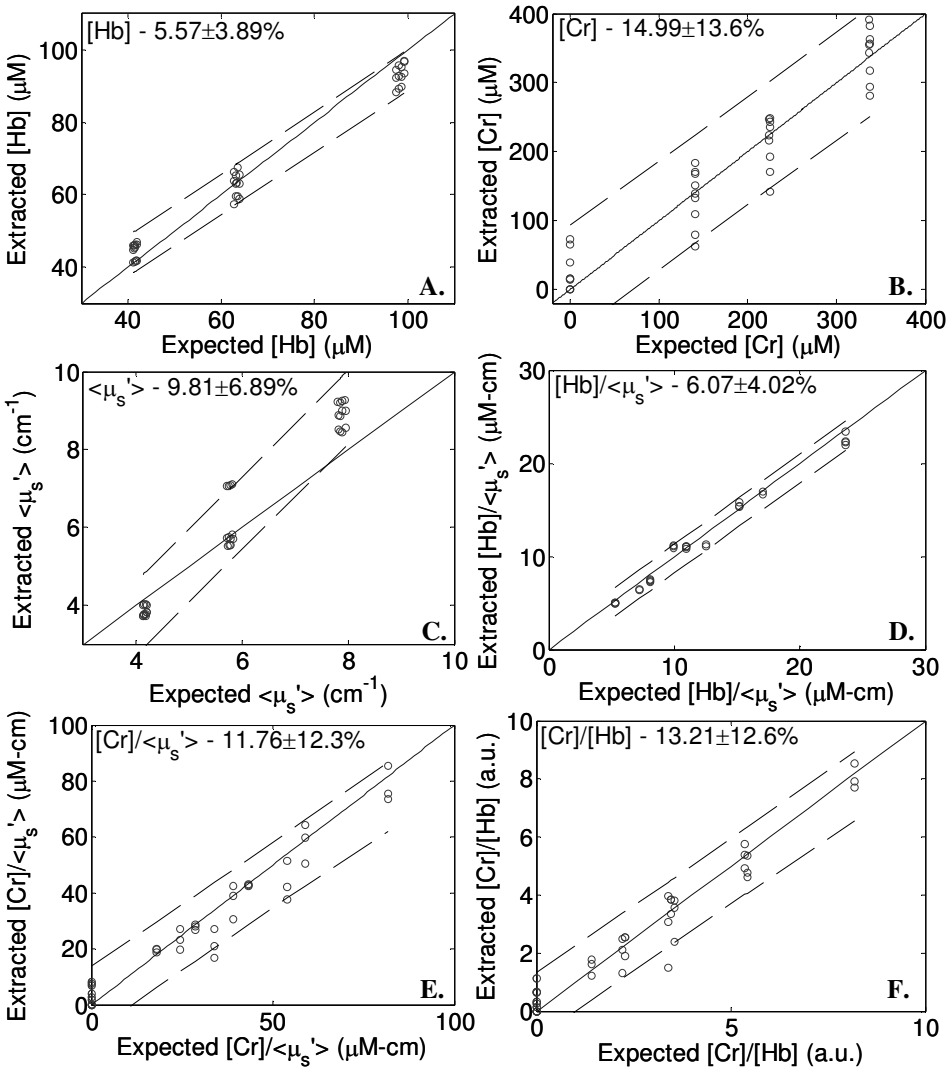

Fig. 5. Average percent error and standard deviation of expected versus extracted plots of Hb concentration (A), Cr concentration (B), $<\mu_s'>$ (C), the ratio of Hb concentration to $<\mu_s'>$ (D), the ratio of Cr concentration to $<\mu_s'>$ (E), and the ratio of Cr to Hb concentration (F). Each circle refers to one phantom extracted from the best reference phantom. The solid line shows the line of perfect agreement between the expected and extracted values and the dashed lines represent the 95% prediction interval.

shows the line of perfect agreement between the expected and extracted values and the dashed lines represent the 95% prediction interval. The average percent error and standard deviation for all 36 phantoms are also shown in each plot. Table 3 shows the bias (mean of the difference between expected and extracted data) and precision (standard deviation of the differences) for each parameter. Taking ratios of the parameters improves the precision of the model and also decreases the percent error. Interestingly in the 48-patient clinical study, the ratios of THb/$<\mu_s'>$ and β-carotene/$<\mu_s'>$ showed the greatest statistical differences between negative and positive margins and these were used in the classification algorithm for margin detection.

#121809 - $15.00 USD Received 21 Dec 2009; revised 19 Mar 2010; accepted 20 Mar 2010; published 1 Apr 2010

Table 3. Mean difference (bias) and standard deviation of differences (precision) between the expected and extracted phantom data.

	Bias	Precision
$<\mu_a>$ (cm^{-1})	0.06	0.40
[Hb] (μM)	0.96	4.33
[Cr] (μM)	–2.80	37.95
$<\mu_s'>$ (cm^{-1})	–0.36	0.71
[Hb]/$<\mu_s'>$ (μM-cm)	0.31	0.75
[Cr]/$<\mu_s'>$ (μM-cm)	1.55	6.26
[Cr]/[Hb] (a.u.)	0.03	0.57

3.4 Optical properties of malignant and non-malignant tissue for sensing depth and cross-talk simulations

The site-level data was separated into malignant and non-malignant tissue types based on pathologic assessment by a board-certified pathologist (JG). This data was used to simulate the sensing depth and cross-talk at the tissue surface. Malignant tissue consisted of positive and close sites, however, for the retrospective characterization of the system only positive sites were used. Non-malignant tissue was divided into adipose, fibro-glandular, and fibro-adipose tissues since these three tissue types make up the majority of the sites measured. Table 4 shows the optical properties at various wavelengths for the different tissue types. The fibro-adipose category was excluded from the sensing depth and cross-talk calculations since the optical properties fall between the optical properties of adipose and fibro-glandular tissue and therefore, the sensing depth and cross-talk of fibro-adipose tissue would be between that of adipose and fibro-glandular tissue.

Table 4. Median values of the extracted absorption and reduced scattering coefficients at specific wavelengths for various tissue types from the site-level data. FA = fibro-adipose, FG = fibro-glandular.

		Malignant	Non-Malignant		
		Positive (n = 10)	Adipose (n = 323)	FA (n = 59)	FG (n = 24)
Absorption Coefficient (cm^{-1})	450 nm	20.34	11.29	10.92	10.50
	500 nm	5.54	3.33	3.26	3.15
	550 nm	9.77	3.29	2.90	3.66
	600 nm	1.42	0.55	0.43	0.92
Reduced Scattering Coefficient (cm^{-1})	450 nm	9.55	7.44	9.20	13.01
	500 nm	9.12	6.92	8.48	12.18
	550 nm	8.82	6.75	7.95	11.98
	600 nm	8.47	6.45	7.82	11.28

3.5 Monte Carlo simulations of sensing depth

The sensing depth of the multi-channel probe was simulated using the extracted optical properties for various tissue types confirmed by site-level pathology. Figure 6 shows an example image of the weighted visiting frequency in each grid at 450 nm and 600 nm for positive tissue. To obtain a single value of weighted visiting frequency at each depth, the weighted visiting frequency was summed across the grids at that depth. This plot also shows how the sensing depth of the probe can change depending on the definition and the percentage used.

#121809 - $15.00 USD Received 21 Dec 2009; revised 19 Mar 2010; accepted 20 Mar 2010; published 1 Apr 2010

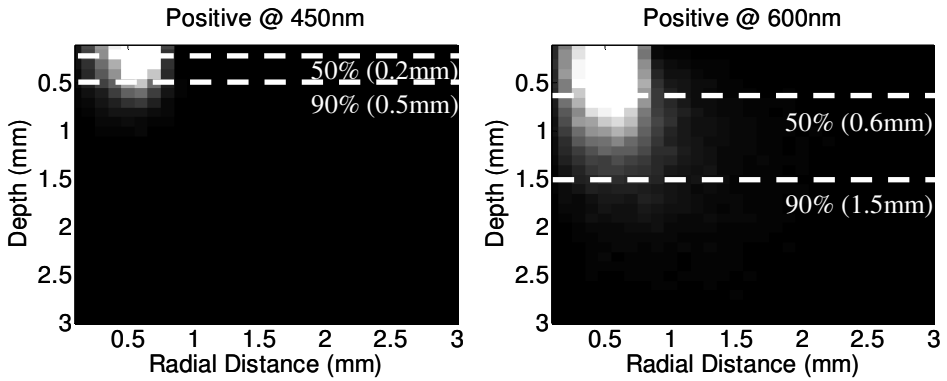

Fig. 6. Example images of the weighted visiting frequency in each grid separated by depth versus radial distance from the center of the illumination fiber. White lines represent the depth where a percentage (50% or 90%) of the detected photon weight distribution is contained within.

Figure 7 shows normalized weighted visiting frequency versus penetration depth for malignant, adipose, and fibro-glandular tissue at the wavelengths of 450 nm and 600 nm to show the full range of the sensing depths across the wavelengths of interest. From the plot it is apparent that sensing depth increases with wavelength, as expected. Although sensing depth was only calculated to be about 1.5-2.2 mm at 600 nm, there are actually photons capable of reaching greater depths, since sensing depth was defined as the depth at which 90% of photons reach before being collected. Therefore, we may be capable of probing tissue slightly deeper than what this figure depicts. Malignant tissue has the shallowest sensing depth while adipose has the greatest. This could be due to the increased number of blood vessels (and hence hemoglobin absorption) present in malignant tissues.

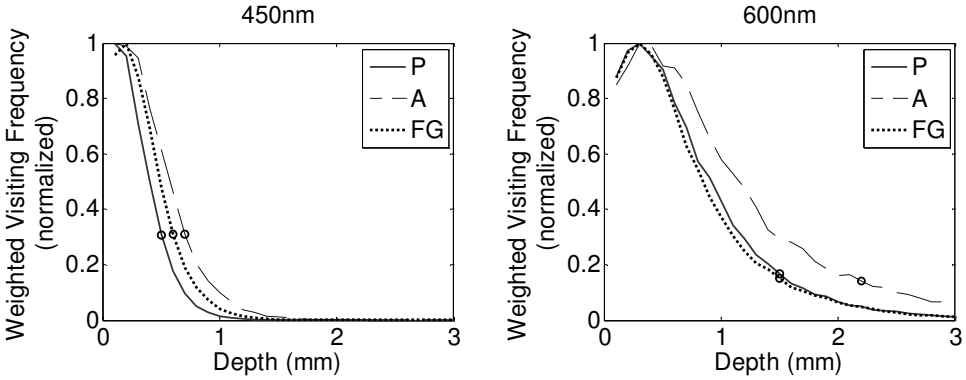

Fig. 7. Simulated weighted visiting frequency as a function of depth for various tissue types (P = positive, A = adipose, FG = fibro-glandular) in a single layer model. Black circles correspond to the depth at which 90% of the photons reach and are collected.

Close margins do not have disease at the surface of the specimen but rather below a layer of benign tissue. To calculate the sensing depth of these close sites adipose or fibro-glandular tissues were considered to be the first layer of the two-layer tissue model, while the malignant tissue was designated as the second layer. Figure 8 shows normalized weighted visiting frequency versus penetration depth for a tissue with an adipose/malignant combination along with a fibro-glandular/malignant combination. The top layer thickness is set at 1 mm. Wavelengths of 450 nm and 600 nm are shown. At 450 nm there is very little difference in the sensing depth for the two different tissue models. However, at 600 nm, there is a greater difference in sensing depth; specifically the adipose/malignant combination has a much larger

#121809 - $15.00 USD Received 21 Dec 2009; revised 19 Mar 2010; accepted 20 Mar 2010; published 1 Apr 2010

sensing depth than the fibro-glandular/malignant combination. Table 5 shows the range of 90% sensing depths from 450 to 600 nm for the single layer model and the two-layer model.

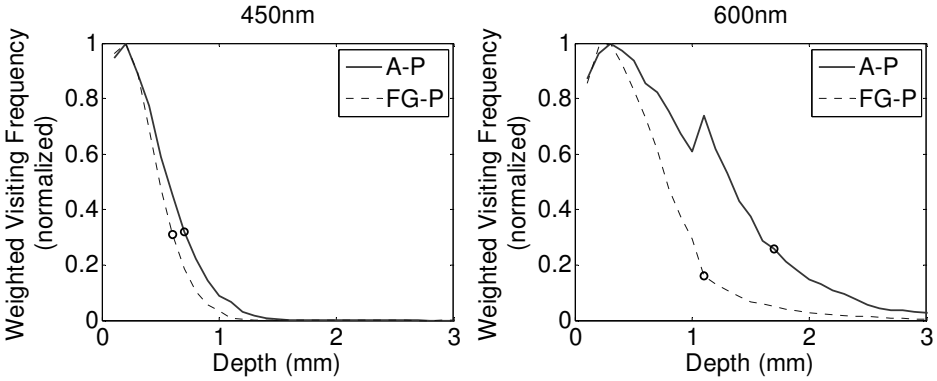

Fig. 8. Simulated weighted visiting frequency as a function of depth for a two-layer tissue model. The first layer is either adipose (A) or fibro-glandular (FG) tissue with a 1 mm thickness and the second layer is positive (P) with a 29 mm thickness. Black circles correspond to the depth at which 90% of the photons reach and are collected.

Table 5. The simulated 90% sensing depth of the 8-channel probe for various tissues in a single layer model and two-layer model. In the two-layer model, the first layer was simulated with a thickness of 1 mm and the second layer with a 29 mm thickness. FG = fibro-glandular.

		90% Sensing Depth (mm)			
		450 nm	500 nm	550 nm	600 nm
Single Layer	Positive	0.50	0.90	0.70	1.50
	Adipose	0.70	1.20	1.20	2.20
	FG	0.60	1.00	0.90	1.50
Two-layer	Adipose-Positive	0.70	1.20	1.00	1.70
	FG-Positive	0.60	0.80	0.70	1.10

3.6 Sensing depth of tissue data

Figure 9 shows the distribution of optical properties stratified by distance of cancerous cells from the inked margin. The extracted μ_a (Fig. 9A,B) and the μ_s' (Fig. 9 C,D) from the site-level tissue data are plotted. For sites where the disease depth was reported, the sites were grouped into different depths: 0 mm (n = 10), 0-1 mm (n = 17), 1-2 mm (n = 10), and greater than 2 mm (n = 406) which are considered negative. A depth of 0 mm is considered positive while depths of 0-1 mm and 1-2 mm are considered close. For each range of depths, μ_a and μ_s' for all sites were plotted at 450 and 600 nm. Absorption is highest for the positive sites and decreases with increasing disease depth. At both 450 nm and 600 nm there is a significant difference in μ_a between disease at 0 mm and disease 1-2 mm away, as well as between 0 mm and negative sites. At 450 nm there is a drop in the median value of μ_a from the positive sites (0 mm) to the other distances. However, the median value is roughly the same for the close (0-1 mm and 1-2 mm) and negative sites, 10.69, 13.78, and 11.09 respectively. At 600 nm, the median value of μ_a also decreases from positive to the other distances. The median value of μ_a also slightly decreases from the close sites (0-1 mm) to the negative sites, 0.68 and 0.54 respectively; and from the close sites (0-1 mm) to the close sites (1-2 mm), 0.68 and 0.51 respectively. At both 450 and 600 nm scattering is highest in the close sites between 0 and 1 mm. Scattering decreases in the close sites 1-2 mm and is lowest in the negative sites. The lower scattering in the positive sites (0 mm) is most likely due to the various tissue types that

#121809 - $15.00 USD Received 21 Dec 2009; revised 19 Mar 2010; accepted 20 Mar 2010; published 1 Apr 2010

make up the close sites. Fibrous tissue shows higher scattering values than malignant tissue as see in Table 4.

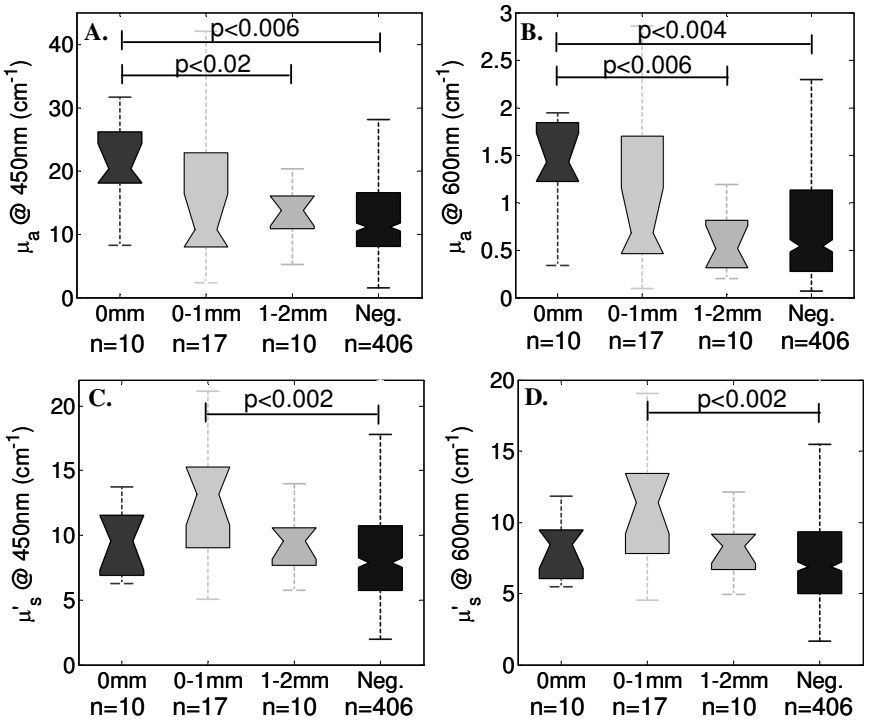

Fig. 9. Box and whisker plots of site-level data. μ_a (A,B) and μ_s' (C,D) coefficients at 450 nm and 600 nm as a function of depth. Positive sites correspond to a depth of 0 mm. Close sites are 0-1 mm and 1-2 mm. Negative sites are greater than 2 mm. P-values are only shown for categories with significant differences. The box represents the median, 25th percentile, and 75th percentile; the whisker represents values within 1.5 times the interquartile range.

3.7 Monte Carlo simulations of cross-talk

The amount of cross-talk between individual channels was calculated for the worst case scenario, a low absorbing tissue for a channel in the center of the multi-channel probe array. Table 6 represents the SNR for 8 different separation distances between channels for the three different tissue types. The optical properties at 600 nm (the wavelength with lowest

Table 6. SNR due to cross-talk calculated using MC simulation. Simulations are based on radius = 0.515 mm for illumination core and 200 μm collection fibers.

	Tissue Type	Positive	Adipose	Fibro-glandular
	μ_a (cm^{-1})	1.42	0.55	0.92
	μ_s' (cm^{-1})	8.47	6.45	11.28
Separation Distance (S.D.)	3 mm	5.48	2.38	5.98
	4 mm	16.58	5.24	18.07
	5 mm	43.80	10.57	49.16
	6 mm	107.81	19.87	125.43
	7 mm	277.27	37.10	287.63
	8 mm	700.97	68.78	635.52
	9 mm	1545.29	114.04	1751.43
	10 mm	3945.91	203.93	3276.21

#121809 - $15.00 USD Received 21 Dec 2009; revised 19 Mar 2010; accepted 20 Mar 2010; published 1 Apr 2010

absorption) from Table 4 were used for the cross-talk simulations. In order to have less than 1% cross-talk between channels an SNR greater than 100 is necessary. The current multi-channel probe has little to no cross-talk and that each channel is capturing information about a specific site. With these optical properties and fiber geometry it is possible to reduce the channel spacing and still minimize cross-talk from adjacent channels.

3.8 Reproducibility

The reproducibility of the clinical data can be seen in Fig. 10. The coefficient of variation (standard deviation / mean) was calculated from 10 serial measurements of the extracted parameters from each site. The median coefficient of variation was calculated over all channels (a total of 32 sites from 4 specimens) for each of the three orientations (Fig. 10). The median coefficient of variation is well below 1 for all extracted parameters (β-carotene, $<\mu_s'>$, THb, β-carotene/$<\mu_s'>$, THb/$<\mu_s'>$, and β-carotene/THb) indicating that there is little deviation from the mean in all measurements. This data also shows that the side orientation is better than the top or bottom orientations with the median coefficient of variation being less than 0.11 for all extracted parameters. This was the orientation used in all of the clinical studies on tumor margins to date.

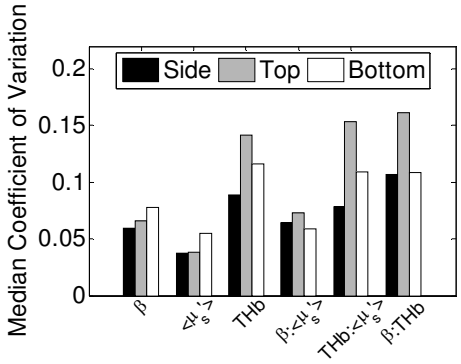

Fig. 10. This plot shows the median coefficient of variation for the 32 sites which was calculated from 10 measurements on 4 separate lumpectomy specimens. β = β-carotene.

4. Discussion

In this paper we have looked at the performance metrics of our clinical instrument for application to intra-operative imaging of partial mastectomy margins. Our measured SNR results show that average SNR across all channels is >100. The channels with the lowest SNR are at the edge of the CCD. There is a possibility that some of the signal collected from these channels is being lost because they are on the edge. A CCD with a few more pixels in the vertical direction could fix this problem.

The phantom study results showed that the extracted data is fairly accurate over a wider range of optical properties than our group has previously explored. Although, the errors are slightly higher than previously reported we do not think it will have much impact on the optical contrast seen between malignant and non-malignant tissues. The percent difference was calculated between the medians of positive and adipose tissue as well as the medians of positive and fibro-glandular tissue. Table 7 compares these percent differences to the average percent errors from the phantom results for the extracted parameters. For all of the parameters, with the exception of β-carotene, the percent difference is much larger than the average percent error in extraction accuracy. The small percent difference between positive and fibro-glandular tissue for β-carotene is probably due to the fact that both malignant tissue and purely fibro-glandular tissue have small amounts of fat present in the measurement site; β-carotene is likely not a good variable to differentiate these two particular tissue types. It is

#121809 - $15.00 USD Received 21 Dec 2009; revised 19 Mar 2010; accepted 20 Mar 2010; published 1 Apr 2010

interesting to note that β-carotene/<μ_s'> was a significant source of contrast in our previously published 48-patient clinical study [2]. However, here it appears that the accuracy with which β-carotene concentrations can be measured does not allow for separation between positive and adipose tissue. We believe this is likely due to propagation of errors in the actual phantom studies. Previously, we have shown that crocin concentrations can be extracted with an accuracy of 4.4% ± 4.0% in a turbid phantom containing hemoglobin, polystyrene spheres, and crocin [30]. In the previous study, the hemoglobin concentration ranged from 6.47 to 11.77 μM and crocin concentration ranged from 0 to 468.50 μM; the ranges for the phantom study in this paper were 41.13-96.88 μM for hemoglobin and 0-337.32 μM for crocin. The higher β-carotene errors seen in the phantom study reported here are likely due to the lower ratio of crocin to hemoglobin concentrations in this set of phantoms. This is supported by the fact that in the current phantom study when the ratio of crocin to hemoglobin concentration increases, the percent error in crocin decreases.

Table 7. Comparison of the percent error in accuracy versus percent differences between tissue types for the extracted parameters.

		% Difference	
	% Error	Positive vs. Adipose	Positive vs. Fibroglandular
[THb]	5.57 ± 3.89	101.18	92.26
[β-carotene]	14.99 ± 13.6	29.91	9.69
<μ_s'>	9.81 ± 6.89	28.11	29.81
[THb]/<μ_s'>	6.07 ± 4.02	92.09	108.27
[β-carotene]/<μ_s'>	11.76 ± 12.3	14.14	88.30
[β-carotene]/[THb]	13.21 ± 12.6	107.67	80.68

Based on the simulations, we have found that the sensing depth of the multi-channel probe ranges from 0.5 to 2.2 mm over the wavelength range of 450-600 nm. There are variations in the literature of the definition of a clear margin. DUMC uses < 2 mm to define a close margin, however, other institutions range from < 1 mm to < 1 cm in their definitions [34], with the majority of pathologists using 2 mm as the pathologic criteria for clear margins [15–19]. With the sensing depth of the probe being ~1-2 mm we hope to compromise between the number of false positives and false negatives. If the mean sensing depth of the probe were 2 mm we may end up with more false positives because the probe could potentially sense positive tissue beyond the depth that pathology samples. In our previous 48-patient clinical study the sensitivity of the device was 82.4% for positive margins and 76.5% for close margins. The comparable sensitivities suggest that although the simulated sensing depth was < 2mm for fibro-glandular and positive tissue, the clinical results suggest that the probe has a sufficient sensing depth that is consistent with the pathologic criterion for clear margins. Compared to touch-prep we are capable of probing tissue at greater depths since this technique only looks at the cells directly at the surface of the margin. In the future, it is possible to change the sensing depth of the probe by altering the probe geometry and/or wavelength range if a greater sensing depth is desired.

With Monte Carlo simulations we showed that cross-talk is minimal (<1%) with the current separation distance between adjacent channels. Therefore, we are confident that the photons captured for a single channel pertain only to the tissue directly underneath it and not from tissue underneath a neighboring channel. With the optical properties found in the *ex vivo* breast tissue it may be possible to decrease the separation distance between channels even further and still maintain <1% cross-talk.

The reproducibility experiment from partial mastectomy specimens showed that in all possible probe orientations the median coefficient of variation is less than 0.17, meaning that all orientations are fairly reproducible. Of the three possible orientations, the side orientation

#121809 - $15.00 USD Received 21 Dec 2009; revised 19 Mar 2010; accepted 20 Mar 2010; published 1 Apr 2010

showed the lowest coefficient of variation for all extracted parameters (<0.11). Therefore, all measurements of partial mastectomy specimens utilized the side orientation. The side orientation may be the most reproducible because it is least affected by pooling of blood. With the desired margin at the top of the box, blood may drain to the bottom of the specimen, thereby decreasing the total hemoglobin concentration over time. With the desired margin on the bottom of the box the opposite effect would take place and total hemoglobin may increase with time. It is also inconvenient to interface the probe to the specimen via the bottom of the box.

The current version of the probe has 8 channels and covers an area of ~2 x 4 cm with 5 mm resolution for 4 consecutive placements of the probe. It takes ~15 seconds to image and 10 seconds to process the data for a single placement of the probe. The majority of margins we have imaged range from 3.1 x 3.1 cm (10 cm^2) to 4.5 x 4.5 cm (20 cm^2). The speed of the system could be significantly improved if it could be designed to cover a margin as large as 20 cm^2 (the large end of margin sizes) with millimeter resolution (comparable to the thickness of each bread loafed pathology specimen) with just a single placement. The number of channels needed to image the largest sized specimen can be determined as follows. The diameter of the sampling area of each channel is typically comparable to the sensing depth and should be between 1 and 2 mm, which is the accepted criterion for clear margins. If there are multiple channels in the device, intuitively, one would minimize spacing between channels and determine the number needed to ensure the entire tissue area is covered. However, because tissue is highly scattering, there should be spacing between channels to minimize cross-talk between adjacent pixels, thus minimizing the sampling of redundant information. To achieve a cross-talk of 5% or less (using the cross-talk of the multi-channel optical spectral imaging system as a benchmark), a minimum center to center channel spacing of 7 mm is desired, as shown in our cross-talk simulation results. Assuming each channel has an active area that is approximately 2 mm in diameter and the center to center channel spacing is 7 mm, a 49 channel device would cover a 4.5 x 4.5 cm (20 cm^2) margin with a single placement of the imaging probe. The scaling of the imaging probe from 8 channels to 49 channels can be readily achieved by incorporating a larger CCD that can resolve more channels, reducing the number of collection fibers to a single fiber per channel to minimize the number of pixels on the CCD occupied by each channel, and by illuminating every other channel at any given time such that with sequential illumination, twice as many channels can be imaged without the issue of cross-talk between adjacent channels.

Acknowledgments

We would like to thank the Duke Comprehensive Cancer Center and the Duke Translational Research Institute for their generous support, the DUMC surgical pathology staff for their help in processing the partial mastectomy specimens and the staff of the Ambulatory Surgery Center for their patience. “The project described was supported by Grant Number 1UL1 RR024128-01 from the National Center for Research Resources (NCRR), a component of the National Institutes of Health (NIH) and NIH Roadmap for Medical Research, and its contents are solely the responsibility of the authors and do not necessarily represent the official view of NCRR or NIH. Information on NCRR is available at http://www.ncrr.nih.gov/. Information on Re-engineering the Clinical Research Enterprise can be obtained from http://nihroadmap.nih.gov/clinicalresearch/overview/translational.asp.” This work was also supported by the following grants: the Department of Defense Breast Cancer Predoctoral Traineeship W81XWH-04-1-0340, the Department of Defense award W81XWH-05-1-036, and National Institute of Health award 1R41CA128160-01. Proposal 1R41CA128160-01 was awarded to Endls Optics that is collaborating with Duke University on this project. Drs. Ramanujam, Brown and Yu and Ms. Junker have financial interest in Endls Optics.

#121809 - $15.00 USD Received 21 Dec 2009; revised 19 Mar 2010; accepted 20 Mar 2010; published 1 Apr 2010